



Exploring diffusion across permeable barriers at high gradients. II. Localization regime



Denis S. Grebenkov

Laboratoire de Physique de la Matière Condensée, CNRS – Ecole Polytechnique, F-91128 Palaiseau, France

ARTICLE INFO

Article history:

Received 12 April 2014

Revised 27 August 2014

Available online 9 September 2014

Keywords:

Bloch–Torrey equation

Permeability

Diffusion

Exchange

Localization

ABSTRACT

We present an analytical solution of the one-dimensional Bloch–Torrey equation for diffusion across multiple semi-permeable barrier. This solution generalizes the seminal work by Stoller, Happer, and Dyson, in which the non-Gaussian stretched-exponential behavior of the pulsed-gradient spin-echo (PGSE) signal was first predicted at high gradients in the so-called localization regime. We investigate how the diffusive exchange across a semi-permeable barrier modifies this asymptotic behavior, and explore the transition between the localization regime at low permeability and the Gaussian regime at high permeability. High gradients are suitable to spatially localize the contribution of the nuclei near the barrier and to enhance the sensitivity of the PGSE signal to the barrier permeability. The emergence of the localization regime for three-dimensional domains is discussed.

© 2014 Elsevier Inc. All rights reserved.

1. Introduction

Diffusion magnetic resonance imaging (dMRI) is a broadly applied non-invasive technique to study anatomical, physiological, and functional properties of biological tissues such as brain, skin, lungs, bones [1–6]. Since cells are separated from the extra-cellular space by semi-permeable cellular membranes, a reliable interpretation of dMRI signals requires accounting for water exchange across these barriers. Numerous works have been devoted to water exchange and aimed to estimate the permeability of cellular membranes [7–39] (see an overview and extended bibliography in [40]).

In most approaches, the dMRI signal is measured (or computed) at relatively small diffusion-encoding gradients g or b -values ($b \propto g^2$) at which the cumulant expansion of the signal can be truncated after the second-order term in the gradient: $S \simeq \exp(-bD_a)$. The estimated effective (or apparent) diffusion coefficient D_a can in turn be related to the permeability. This second-order approximation (known also as the Gaussian phase approximation), fails at high gradients [3,41,42]. Many models have been proposed to remedy this failure and to get a simple fitting formula for the dMRI signal in an extended range of applied gradients: kurtosis model based on the cumulant expansion [43,44] and phenomenological models such as bi-exponential model [45–49], stretched-exponential model [50,51], and distributed models [52,53]. These models start from the Gaussian dMRI signal and modify it in a convenient way. For instance, two Gaussian signals are superimposed in the

bi-exponential model, while the next-order term of the cumulant expansion is included in the kurtosis model. Although these models are often successful in fitting experimental data on a broader range of gradients, none of them has addressed the theoretical question how the dMRI signal is indeed modified at high gradients.

In the seminal paper, Stoller, Happer, and Dyson predicted the emergence of the so-called localization regime at high gradients [54]. Since the motion of the nuclei near an impermeable boundary is more restricted, their local transverse magnetization is less attenuated, as compared to the bulk magnetization. This effect, known as diffusive edge enhancement, has been observed experimentally [55] (see also [56]). Stoller et al. provided a *non-perturbative* analysis of the one-dimensional Bloch–Torrey equation and obtained non-Gaussian asymptotic behavior of the dMRI signal at high gradients: $\ln S(g) \propto g^{2/3}$, in sharp contrast to the usual Gaussian form $\ln S(g) \propto g^2$ [54]. Moreover, de Swiet and Sen extended this non-Gaussian behavior to generic geometrical restrictions [57] while Hürlimann and co-workers have confirmed these theoretical predictions experimentally [58] (see reviews [3,59] for details).

In the present work, we extend the concept of the transverse magnetization localization to *semi-permeable* barriers. Applying high gradients, one can eliminate the contribution from bulk diffusion in order to enhance the relative contribution of the signal coming uniquely from the nuclei near the barriers. In other words, high gradients may serve as efficient “contrast agents” to enhance interfaces. Moreover, the signal attenuation becomes very sensitive to the permeability, as faster exchange yields much stronger signal attenuation. The idea of removing the bulk water contribution from the signal has been earlier suggested by Åslund et al. by

E-mail address: denis.grebenkov@polytechnique.edu

adding a “diffusion filter”: a preliminary pulsed-gradient spin-echo (PGSE) block that selectively removes the transverse magnetization of the extracellular water [34]. In the earlier paper [40], we also explored the idea of enhancing the contribution from a semi-permeable barrier under the narrow pulse approximation (NPA) when the PGSE signal could be related to the diffusion propagator. In particular, we showed that the contribution from the barrier can be enhanced by adaptively changing the gradient intensity with the diffusion time. Here, we relax the limitations of the NPA and provide the exact non-perturbative solution of the one-dimensional Bloch–Torrey equation in the presence of a semi-permeable barrier. We derive then an explicit asymptotic behavior of the PGSE signal and show that this analysis is also applicable to multiple well-separated barriers. The derived formulas can potentially be used for fitting experimental signals and thus estimating the permeability. Varying diffusive exchange, one can explore the transition between non-Gaussian localization regime at low permeability and Gaussian regime at high permeability. In this way, one can better understand the mechanisms of the transverse magnetization localization near barriers, the failure of the Gaussian phase approximation, and the role of diffusive exchange across the barriers. The validity of the localization regime for three-dimensional domains is also discussed.

The paper is organized as follows. In Section 2, we formulate the one-dimensional Bloch–Torrey equation in the presence of a single semi-permeable barrier and present its rigorous solution, for both free induction decay (FID) and PGSE sequence. In particular, we establish the localization of the transverse magnetization near the barrier and retrieve the long-time asymptotic behavior: $\ln S(g) \propto g^{2/3}$, with the proportionality factor depending on the permeability. In Section 3, we illustrate theoretical results and discuss their advantages, limitations, and applications: characteristic scales, localization of the transverse magnetization, transition from Gaussian to stretched-exponential behavior, higher sensitivity of the PGSE signal to permeability at high gradients, danger of phenomenological models, the effect of multiple barriers, and the validity of the localization regime for three-dimensional domains. At the end of Section 3, we summarize the conditions under which the localization regime emerges, its relevance for dMRI, and the related mathematical and physical challenges. Most mathematical details are moved to Supplementary Materials (SM) which contain a didactic derivation of the analytical (non-perturbative) solution for a single semi-permeable barrier, an extension to an arbitrary configuration of multiple barriers, and summary of numerical aspects [60].

2. Theory

In this section, we formulate consider the one-dimensional Bloch–Torrey equation for a single semi-permeable barrier (Section 2.1), discuss its analytical (non-perturbative) solution (Section 2.2), and establish the exact spectral form of the PGSE signal and its non-Gaussian stretched-exponential asymptotic behavior at long times (Section 2.3). This section presents only the main steps and summarizes major results while mathematical details are provided in SM [60]. A reader who is less interested in theoretical background, may skip this section and move directly to discussions in Section 3.

2.1. Bloch–Torrey equation

Following Stoller, Happer, and Dyson, we consider the one-dimensional Bloch–Torrey equation [61]:

$$\frac{\partial}{\partial t} M_t(x|g) = \left(D \frac{\partial^2}{\partial x^2} + i\gamma g f(t)x \right) M_t(x|g), \quad (1)$$

where $M_t(x|g)$ is the (complex-valued) transverse magnetization, D is the (self-)diffusion coefficient, γ the gyromagnetic ratio (e.g., $\gamma = 2.675 \cdot 10^8$ rad/s/T for water protons), and g and $f(t)$ are the strength and normalized temporal profile of the applied magnetic field gradient. The time-independent gradient (with $f(t) \equiv 1$) describes free induction decay (FID), while a standard PGSE sequence with two rectangular gradient pulses of opposite signs is given by

$$f(t) = \begin{cases} 1 & 0 < t < \delta, \\ -1 & \Delta < t < \Delta + \delta, \\ 0 & \text{otherwise,} \end{cases} \quad (2)$$

where δ is the duration of pulses, and Δ is the diffusion time between the starting of each pulse. We first focus on the time-independent gradient ($f(t) \equiv 1$) and then extend results to the PGSE sequence.

The Bloch–Torrey Eq. (1) describes the evolution of the transverse magnetization $M_t(x|g)$ from an initial state, $M_0(x|g) = \rho(x)$, which is often considered to be uniform over the voxel after the exciting 90° rf pulse. The first term in the right-hand side of Eq. (1) describes diffusion of the nuclei, while the second term incorporates their dephasing due to the gradient (note that the second term is often written with the negative sign; here, we keep Stoller's notation for convenience, given that the sign does not affect the results for spin echoes). Throughout the paper, we ignore the T_2^* relaxation caused by molecular interactions (spin–spin relaxation) and local magnetic field non-uniformities. If this relaxation is homogeneous, its contribution e^{-t/T_2^*} can be factored out and ignored by considering the signal attenuation from a reference signal (without applied gradient).

Although the uniform excitation over the voxel is experimentally performed, it is instructive to consider the transverse magnetization produced by the nuclei started from a fixed source point y . The resulting transverse magnetization for time-independent gradient is called the propagator, $G(x, y; t|g)$, or the Green's function of the Bloch–Torrey equation:

$$\frac{\partial}{\partial t} G(x, y; t|g) = \left(D \frac{\partial^2}{\partial x^2} + i\gamma g x \right) G(x, y; t|g), \quad (3)$$

with the initial condition

$$G(x, y; t=0|g) = \delta(x - y), \quad (4)$$

where $\delta(x)$ is the Dirac distribution. From the propagator, the transverse magnetization $M_t(x|g)$ is obtained by integrating $G(x, y; t|g)$ over y with the prescribed initial density, while the FID is given by the second integral over x with the voxel pick-up function.

For unrestricted diffusion, the propagator $G_0(x, y; t|g)$ is well known [54]

$$G_0(x, y; t|g) = \frac{1}{\sqrt{4\pi Dt}} \times \exp \left(-\frac{(x-y)^2}{4Dt} + i\gamma g t \frac{x+y}{2} - \frac{D\gamma^2 g^2 t^3}{12} \right). \quad (5)$$

Note that Eq. (5) reduces to the standard Gaussian propagator at $g = 0$. No other exact explicit solution is available, even for the one-dimensional problem over the semi-axis (with a single endpoint). For this reason, most of earlier theoretical investigations relied either on the Gaussian phase approximation (that relates the PGSE signal to the second moment of dephasing), or on the narrow pulse approximation [40] (that relates the PGSE signal to a purely diffusive propagator by choosing specific gradient profile) [3]. The seminal work by Stoller et al. [54] presents a notable exception, in which the propagator was derived for one-dimensional domains with one or two reflecting endpoints (see SM [60]).

We extend the non-perturbative analysis to the whole line with a single semi-permeable barrier at the origin that separates the positive and negative semi-axes. Two boundary conditions at the barrier represent the flux conservation across the barrier, and the drop of transverse magnetization due to permeation through the barrier:

$$\begin{aligned} \left(D \frac{\partial}{\partial x} G(x, y; t|g) \right)_{|x=0^+} &= \left(D \frac{\partial}{\partial x} G(x, y; t|g) \right)_{|x=0^-} \\ &= \kappa [G(0^-, y; t|g) - G(0^+, y; t|g)], \end{aligned} \quad (6)$$

where the approaches to the barrier ($x = 0$) from the negative and from the positive axes are distinguished explicitly by 0^\pm . Here κ is the permeability, and the same diffusion coefficient D is taken on the positive and negative semi-axes (one can also derive results for different diffusion coefficients, see SM [60]). The limiting case $\kappa = 0$ describes two isolated compartments (with zero diffusive flux at $x = 0$). The opposite limit of infinitely permeable barrier, $\kappa = \infty$, corresponds to absence of a barrier and implies the continuity of the propagator $G(x, y; t|g)$ at $x = 0$: $G(0^-, y; t|g) = G(0^+, y; t|g)$. In intermediate cases ($0 < \kappa < \infty$), the propagator exhibits a discontinuity at the barrier due to its “resistance” to exchange.

2.2. Exact (non-perturbative) solution

Following Ref. [54], we derive in SM [60] the exact representation of the propagator $G(x, y; t|g)$ satisfying the Bloch–Torrey Eq. (3), the initial condition (4), and the boundary conditions (6). For $x > 0$ and $y > 0$, one gets

$$\begin{aligned} G(x, y; t|g) &= \lambda \sum_{n=-\infty}^{\infty} c_n \exp(D\lambda^2 t s_n) \\ &\quad \text{Ai}(e^{-2\pi i/3}(i\lambda x - s_n)) \text{Ai}(e^{-2\pi i/3}(i\lambda y - s_n)), \end{aligned} \quad (7)$$

where $\text{Ai}(z)$ is the Airy function,

$$\ell_g = (\gamma g/D)^{-1/3}, \quad \lambda = 1/\ell_g = (\gamma g/D)^{1/3} \quad (8)$$

are the gradient length and its inverse, c_n are dimensionless coefficients for which explicit formulas are derived in SM [60] (similar expansions are applicable for both positive and negative x and y). In Eq. (7), s_n are the (complex-valued) poles of the Laplace-transformed Green's function of the Bloch–Torrey equation. These poles satisfy the equation

$$f(s) + h = 0, \quad (9)$$

with

$$h = \frac{\kappa}{D\lambda} = \frac{\kappa}{D^{2/3}(\gamma g)^{1/3}}, \quad (10)$$

and

$$f(s) = 2\pi \text{Ai}'(-e^{-2\pi i/3}s) \text{Ai}'(-e^{2\pi i/3}s), \quad (11)$$

where $\text{Ai}'(z)$ is the derivative of the Airy function. For convenience, we associate complex conjugate pairs of solutions as $s_{-n} = s_n^*$. As discussed below, the real part of s_n is negative so that there is no minus sign in the exponential function in Eq. (7).

Several comments are in order:

- (i) The propagator in Eq. (7) depends on four dimensionless parameters: starting and arrival positions $y\lambda$ and $x\lambda$, time $D\lambda^2 t$, and permeability $h = \kappa/(D\lambda)$, with the inverse gradient length λ from Eq. (8). While the first three parameters are obtained just by rescaling y, x and t by characteristic length and time scales, the last parameter h determines implicitly all spectral properties, as discussed below.

- (ii) The spatial dependence of the propagator enters through the Airy functions which rapidly decay as $|x|$ or $|y|$ become large compared to the gradient length ℓ_g because [62]

$$\text{Ai}(z) \sim \frac{\exp(-\frac{2}{3}z^{3/2})}{2\sqrt{\pi}z^{1/4}} \quad (|\arg z| < \pi, |z| \gg 1). \quad (12)$$

As a consequence, the contribution from distant source points (i.e., when $|y| \gg \ell_g$) is negligible. This is precisely the effect of localization of the transverse magnetization near the barrier when only the nuclei around the barrier (within a distance ℓ_g) do contribute to the signal at high gradients. This localization effect disappears at small gradients at which ℓ_g becomes large. In turn, higher gradients reduce the gradient length ℓ_g and thus allow for a better spatial localization of the barriers.

At the same time, the nuclei far from the barrier do not “feel” its presence so that one expects

$$G(x, y; t|g) \approx G_0(x, y; t|g), \quad (13)$$

for $|x| \gg \sqrt{Dt}$ or $|y| \gg \sqrt{Dt}$, where the propagator $G_0(x, y; t|g)$ for unrestricted diffusion is given by Eq. (5). This property illustrates challenges in the analysis of series representations such as Eq. (7). In fact, although each Airy function in the series exhibits the asymptotic behavior (12), the whole series may decay differently. Note that the arguments of Airy functions are complex so that the asymptotic relation (12) may also represent a rapid growth in some regions of the complex plane.

- (iii) All poles s_n have strictly negative real part, i.e., $\text{Re}\{s_n\} < 0$, so that each term in Eq. (7) exhibits exponential decay with time t . Introducing the gradient time as

$$\tau_g = 1/(D\lambda^2) = D^{-1/3}(\gamma g)^{-2/3}, \quad (14)$$

one can define the long-time limit as $t \gg \tau_g$ when the asymptotic behavior of the propagator is dominated by two complex conjugate terms with the smallest decay rate $|\text{Re}\{s_1\}|$ (for indices $n = 1$ and $n = -1$). As a consequence, the propagator exponentially decays with time, in sharp contrast to the free propagator in Eq. (5), whose temporal decay is much faster: $\sim \exp(-\text{const } t^3)$. On the contrary, the analysis of the short-time behavior of the propagator involves (infinitely) many terms in the series (7). In a first approximation, the short-time behavior is similar to that of the propagator $G_0(x, y; t|g)$ for unrestricted diffusion.

- (iv) The propagator exhibits a complicated dependence on the gradient strength g which enters through λ, h (and thus s_n), and c_n . For large g (or λ), the major dependence comes from the exponential factor $\exp(D\lambda^2 t s_1)$. In the opposite limit of small g (i.e., $\lambda \rightarrow 0$), (infinitely) many terms in the series (7) do contribute. The formal derivation of this asymptotic behavior requires a substantial analysis while the limit $G(x, y; t|0)$ at $g = 0$ can be found independently, for purely diffusive problem:

$$\begin{aligned} G(x, y; t|0) &= \frac{\exp\left(-\frac{(x-y)^2}{4Dt}\right) + \exp\left(-\frac{(x+y)^2}{4Dt}\right)}{\sqrt{4\pi Dt}} \\ &\quad - \frac{\kappa}{D} \exp\left(\frac{2\kappa}{D}(y+x+2\kappa t)\right) \text{erfc}\left(\frac{y+x+4\kappa t}{2\sqrt{Dt}}\right), \\ G(x, y; t|0) &= \frac{\kappa}{D} \exp\left(\frac{2\kappa}{D}(y-x+2\kappa t)\right) \text{erfc}\left(\frac{y-x+4\kappa t}{2\sqrt{Dt}}\right), \end{aligned} \quad (15)$$

where $\text{erfc}(z)$ is the complementary error function, and the first (resp., second) relation corresponds to $x > 0$ (resp. $x < 0$). These expressions are valid for $y > 0$, while their

extension to $y < 0$ is straightforward: $G(-x, -y; t|0) = G(x, y; t|0)$.

- (v) The permeability κ defines in Eq. (10) the dimensionless parameter h and thus determines the poles s_n . In particular, the decay rate $|\text{Re}\{s_1\}|$ of the propagator in the long-time limit is sensitive to the permeability and can thus potentially be used to estimate this quantity. Fig. 1 shows the dependence of the real part of the first three poles s_n on h . For small h , one gets (see SM [60]):

$$s_n = -e^{2\pi i/3} a'_n + \frac{e^{\pi i/6}}{a'_n} h + O(h^2), \quad (16)$$

where a'_n are the (tabulated) zeros of $\text{Ai}'(z)$: $a'_1 \approx -1.0188$, $a'_2 \approx -3.2482$, etc. In particular, one has $-\text{Re}\{s_1\} \approx 0.51 + 0.85h$, $-\text{Re}\{s_2\} \approx 1.62 + 0.27h$, etc. This asymptotic relation is illustrated in Fig. 1 by crosses.

At large h , the real part of s_n logarithmically diverges to $-\infty$. In a first approximation, one obtains (see SM [60])

$$\text{Re}\{s_n\} \simeq -\left(\frac{3}{4} \ln h\right)^{2/3}. \quad (17)$$

This relation, which is shown by circles in Fig. 1, is asymptotically the same for all poles. Note that the limit $g \rightarrow 0$ formally corresponds to $h \rightarrow \infty$ for any nonzero permeability κ . Although the poles s_n diverge logarithmically as $g \rightarrow 0$, the propagator reaches the well defined limit (15).

As discussed below, the imaginary parts of s_n are not relevant for the signal attenuation but may be responsible for its oscillating features.

2.3. PGSE signal

Knowing the spectral representation (7), one can compute the spin-echo propagator for any PGSE sequence with a piecewise constant gradient as convolution of multiple constant-gradient propagators $G(x, y; t|g)$. The integral of the resulting spin-echo propagator with the initial density $\rho(y)$ over y yields the transverse magnetization, while the second integral with the voxel pick-up function $\tilde{\rho}(x)$ over x gives the PGSE signal (see SM [60] for details). For instance, for a standard Stejskal–Tanner PGSE sequence from Eq. (2) with two rectangular gradient pulses of duration δ , separated by the diffusion time Δ , the PGSE signal can be formally written as

$$S(g) = \lambda^{-1} \sum_{n, n'=-\infty}^{\infty} C_{n, n'}^S(\Delta - \delta) \exp(D\lambda^2(s_n + s_{n'}^*)\delta), \quad (18)$$

where the coefficients $C_{n, n'}^S(\Delta - \delta)$ depend in $\Delta - \delta$, gradient g , and permeability κ (see SM [60]). Although Eq. (18) is exact, its practical use is limited because of the computational difficulties in getting many coefficients $C_{n, n'}^S$.

In the long-time limit $\delta \gg \tau_g$, the dominating contribution comes from four terms $n = \pm 1$, $n' = \pm 1$ with the smallest decay rate $2|\text{Re}\{s_1\}|$. One retrieves therefore the exponential decay of the Stejskal–Tanner PGSE signal and its characteristic $g^{2/3}$ dependence on the gradient strength:

$$S(g) \simeq \zeta \frac{\rho_0}{(\gamma g/D)^{1/3}} \exp\left(-(\gamma g)^{2/3} D^{1/3} 2\delta |\text{Re}\{s_1\}|\right), \quad (19)$$

where the prefactor ζ includes four coefficients $C_{\pm 1, \pm 1}^S$ which are reduced to two terms:

$$\rho_0 \zeta = 2C_{1,1}^S(\Delta - \delta) + 2\text{Re}\left\{C_{1,-1}^S(\Delta - \delta) \exp\left(i(\gamma g)^{2/3} D^{1/3} 2\delta \text{Im}\{s_1\}\right)\right\}, \quad (20)$$

and ρ_0 characterizes the initial density (e.g., $\rho_0 = 1/(2R)$ for a uniform initial density over an interval $[-R, R]$). Strictly speaking, the prefactor ζ depends on all the parameters: $\gamma, g, \Delta, \delta, \kappa$, and even on the form of the initial density $\rho(y)$. In the limit $h = 0$, the coefficient $C_{1,-1}^S$ vanishes, yielding $\zeta = 2C_{1,1}^S(\Delta - \delta)/\rho_0$. For instance, for the particular case of a Hanh echo sequence with $\Delta = \delta$ and the uniform initial density, the numerical value $\zeta \approx 5.8841$ was first reported by Hürlimann et al. [58]. Fig. 2a shows both coefficients $C_{1,1}^S$ and $C_{1,-1}^S$ as functions of the dimensionless permeability h for the Hanh echo sequence. At small h , the coefficient $C_{1,1}^S$ is almost constant while $C_{1,-1}^S$ is negligible. When h increases, both coefficients grow, and the relative weight of $C_{1,-1}^S$ increases that results in time dependence and oscillating character of ζ in Eq. (20). These features are illustrated in Fig. 2b which shows ζ as a function of g for three fixed permeabilities. One can see that ζ is almost constant for small permeabilities, and it varies slowly with the gradient for larger permeabilities.

For comparison, we recall the classical Stejskal–Tanner expression for the PGSE signal attenuation due to unrestricted diffusion [64]:

$$S_0(g) = e^{-D\gamma^2 g^2 \delta^2 (\Delta - \delta/3)} = e^{-(\delta/\tau_g)^3 (\Delta/\delta - 1/3)}. \quad (21)$$

For large gradients and/or long times, this Gaussian signal decays much faster than Eq. (19).

We emphasize that the PGSE signal in Eq. (19) is proportional to the density ρ_0 which is equal to $1/(2R)$ for the uniform initial distribution over an interval $[-R, R]$. In [40], the PGSE signal under the narrow pulse approximation was shown to be the sum of the Gaussian term for unrestricted diffusion and the contribution from a semi-permeable barrier which was also proportional to the density $1/(2R)$. Here, the Gaussian term is negligible because of too high gradients so that the barrier contribution strongly dominates. The rapid decay of the transverse magnetization in distant regions allows one to extend the above result to multiple well-separated barriers. If the voxel of size $2R$ contains n well-separated identical barriers (with the same permeability), each of them provides the same contribution to the signal. The total signal is therefore given by Eq. (19), in which the density ρ_0 is replaced by $1/\ell_b$, where $\ell_b = 2R/n$ is the average inter-barrier distance. As a consequence, the localization regime can potentially be used to estimate this important parameter.

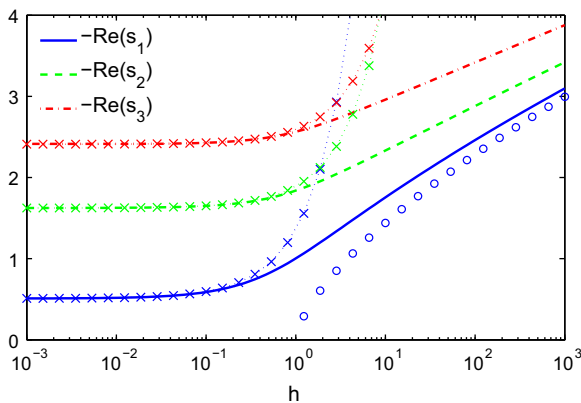


Fig. 1. The real part of the first three poles s_n satisfying $f(s_n) + h = 0$, as functions of h . The small- h approximation (16) is shown by crosses while the large- h asymptotic relation (17) is shown by circles. Small h correspond to low permeabilities and/or high gradients.

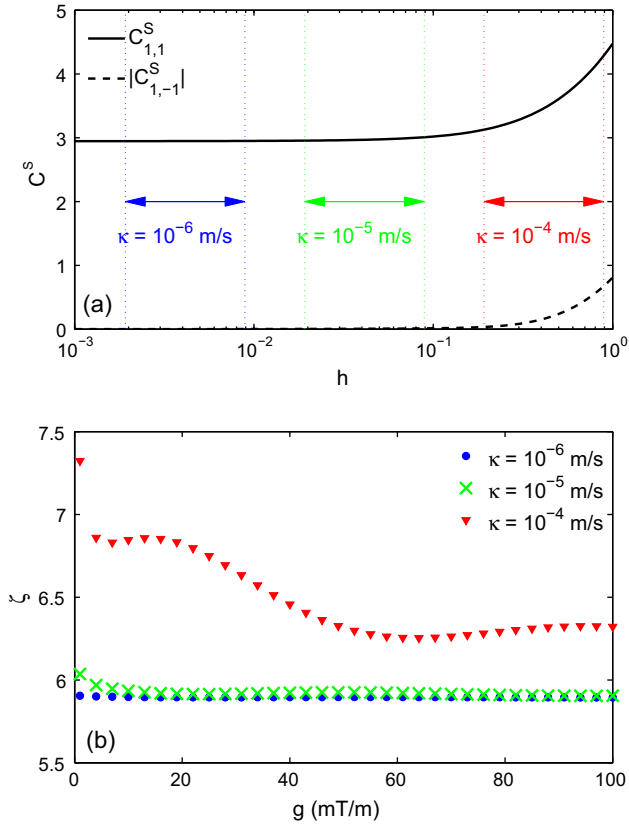


Fig. 2. (a) Two coefficients $C_{1,1}^S$ and $C_{1,-1}^S$ from Eq. (18) as functions of the dimensionless permeability h . Three zones delimited by vertical dotted lines indicate variations of h that correspond to the gradient range between 1 and 100 mT/m and three permeabilities κ according to Eq. (10), with $D = 2.3 \cdot 10^{-9}$ m²/s. (b) The coefficient ζ as a function of g , for three permeabilities κ . This coefficient was computed from $C_{1,1}^S$ and $C_{1,-1}^S$ according to Eq. (20) for $D = 2.3 \cdot 10^{-9}$ m²/s, $\Delta = \delta = 50$ ms, and uniform initial density $\rho(y)$ over the interval $[-R, R]$, with $R = 50$ μ m (note that ζ does not depend on the particular choice of R if R is large as compared to the gradient length).

3. Discussion

3.1. Characteristic scales

The exact solution (7) of the Bloch–Torrey equation identifies two characteristic scales: the gradient time τ_g from Eq. (14) and the gradient length ℓ_g from Eq. (8), as first suggested by de Swiet and Sen [57]. For water diffusion (with $D = 2.3 \cdot 10^{-9}$ m²/s), τ_g [resp., ℓ_g] varies from 183 ms [resp., 20 μ m] at $g = 1$ mT/m to 1.8 ms [resp., 2 μ m] at $g = 1000$ mT/m, as illustrated in Fig. 3. One can see that a large gradient variation by three orders of magnitude implies only a tenfold change in the gradient length because $\ell_g \propto g^{-1/3}$. In turn, the gradient time exhibits stronger variations as $\tau_g \propto g^{-2/3}$.

It is instructive to compare ℓ_g to three other length scales:

- (i) The diffusion length $\sqrt{2D\Delta}$ varies from 6.8 to 21 microns as Δ changes from 10 to 100 ms. This range is comparable to variations of the gradient length ℓ_g .
- (ii) The permeation length D/κ varies from two millimeters at $\kappa = 10^{-6}$ m/s (considered as almost impermeable barrier) to 23 μ m at $\kappa = 10^{-4}$ m/s (considered as almost fully permeable barrier), see discussion about the water permeability for various biological membranes in [40]. The ratio between the permeation and gradient lengths defines in Eq. (10) the dimensionless parameter h which determines the solutions s_n of Eq. (9) and all other spectral parameters. Since the

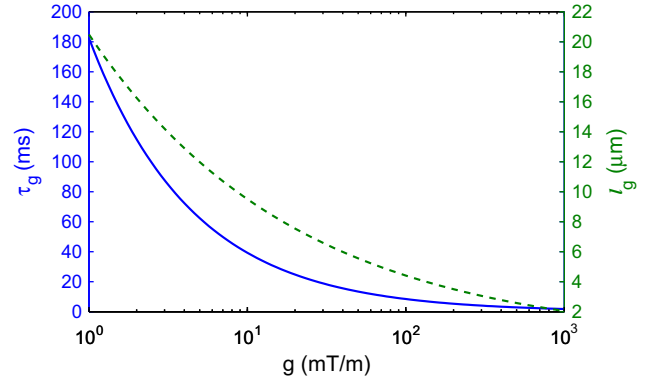


Fig. 3. Gradient time τ_g (solid blue curve, left vertical axis) and gradient length ℓ_g (dashed green line, right vertical axis), versus g for water diffusion (with $D = 2.3 \cdot 10^{-9}$ m²/s). The localization regime becomes dominant for pulse duration $\delta \gg \tau_g$, in which case the transverse magnetization is negligible at distances $|x| \gg \ell_g$ from the barrier.

permeation length remains larger (and typically much larger) than the gradient length ℓ_g , h stays below 1 for a relevant range of gradients.

- (iii) The size of cells and extracellular regions can vary from submicrons (e.g., the diameter of dendrites) to 10 μ m (e.g., the soma of neurons) and much larger values in plant cells. Since these sizes are comparable to ℓ_g , the effects of transverse magnetization localization near membranes and the consequent non-Gaussian signal attenuation at high gradients can be relevant for relatively large cells.

The PGSE signal for unrestricted diffusion is often expressed in terms of the b -value as $S_0 = e^{-bD}$, with $b = \gamma^2 g^2 \delta^2 (\Delta - \delta/3)$ for standard rectangular pulses described by Eq. (2). The b -value can be expressed through the gradient time as $bD = (\delta/\tau_g)^3 (\Delta/\delta - 1/3)$, where the dimensionless factor $\Delta/\delta - 1/3$ accounts for the particular form of this sequence (gradient form or temporal profile). Typical b -values up to 4000 s/mm² used for modern brain dMRI [6] require either long diffusion times Δ (that would slow down the overall acquisition protocol) or long gradient pulse duration δ or large gradients (i.e., small τ_g). For instance, the PGSE sequence with $\Delta = 53$ ms, $\delta = 47$ ms, and g up to 34 mT/m was used in [63] to get b -values up to 6800 s/mm². At this maximal gradient, the gradient time τ_g is around 17 ms that makes δ threefold larger than τ_g and suggests the potential relevance of the localization regime (note that the PGSE signal for unrestricted diffusion would be extremely small for these parameters). In what follows, we choose $\Delta = \delta = 50$ ms to illustrate theoretical results. For comparison, we will also present results for a shorter PGSE sequence with $\Delta = \delta = 10$ ms, in which case much stronger gradients are required to get significant signal attenuation. Although such gradients are not currently implemented (or even permitted) on medical equipment, they are available on small-bore scanners.

3.2. Numerical simulations

In spite of the exact character of theoretical results from Section 2, numerical calculation of the PGSE signal through its spectral representation (18) is rather tedious (see SM [60] for details). In order to overcome technical difficulties, we resort to a numerical tool based on the matrix formalism in which the Bloch–Torrey equation is projected onto the Laplace operator eigenfunctions and the resulting linear system of first-order differential equations is truncated and solved in a matrix form [3,65–69]. For this purpose, we consider an interval $[-L, L]$ with two reflecting endpoints at $\pm L$

and a semi-permeable barrier at the center. The uniform initial distribution is set over the whole interval $[-L, L]$. The effect of the artificially introduced reflecting barriers can be made negligible by integrating the transverse magnetization over a smaller subinterval $[-R, R] \subset [-L, L]$ so that the contribution of the nuclei affected by the endpoints is excluded from the signal (see SM [60] for details). Since the Laplacian eigenbasis is explicitly known for an interval with single or multiple barriers, the matrix formalism provides a rapid and accurate numerical tool for computing propagators, magnetizations, and signals [3,70,71]. The matrix formalism package for multilayered structures has been implemented in Matlab and is available on request. We set $D = 2.3 \cdot 10^{-9} \text{ m}^2/\text{s}$ for water diffusion at room temperature and consider a broad range of permeabilities, as discussed in Section 3.1. The standard PGSE sequence with two rectangular pulses is applied, with either $\Delta = \delta = 50 \text{ ms}$ and gradients up to 80 mT/m (with the maximal b -value 4770 s/mm^2), or $\Delta = \delta = 10 \text{ ms}$ and gradients up to 800 mT/m (with the maximal b -value 3800 s/mm^2). By default we choose $L = 100 \mu\text{m}$ and $R = 50 \mu\text{m}$ so that the distance to reflecting endpoints, $L - R$, is much larger than the diffusion length $\sqrt{2D\Delta}$. We checked numerically that very similar results were obtained for larger L , i.e., the presence of reflecting endpoints can indeed be ignored. In other words, restricted diffusion in this interval is made equivalent to diffusion over the whole line with a single semi-permeable barrier considered in Section 2.

3.3. Localization of the transverse magnetization

Fig. 4 shows the absolute value of the transverse magnetization $M_{2\Delta}(x|g)$ at the echo time 2Δ for two gradients: $g = 5 \text{ mT/m}$ and $g = 50 \text{ mT/m}$. For convenience, the dimensional magnetization (in units m^{-1}) is normalized by its initial value $M_0 = 1/(2L)$. For the small gradient $g = 5 \text{ mT/m}$ (Fig. 4a), the weak dephasing of the nuclei slightly perturbs the initial uniform distribution, resulting in the transverse magnetization which slowly varies along the sample. As expected, higher (less attenuated) values are observed near the barrier and two endpoints due to slower diffusion. More attenuated values are found in the most distant regions from the barriers (i.e., around $\pm L/2$). At the highest permeability $\kappa = 10^{-3} \text{ m/s}$ (shown by full circles), diffusion is nearly Gaussian and is close to the unrestricted case, for which the normalized magnetization is flat: $\exp(-D\gamma^2 g^2 (2\delta)^3 / 12)$ (shown by horizontal solid line). The transverse magnetization near the semi-permeable barrier exhibits a weak dependence on the permeability.

The situation changes at the higher gradient $g = 50 \text{ mT/m}$ for which the Gaussian phase approximation fails. In this regime, the transverse magnetization is localized near the barrier and endpoints (Fig. 4b). At very low permeability ($\kappa = 10^{-6} \text{ m/s}$), the barrier separates the interval into two almost isolated subintervals. The transverse magnetization is preserved around the barrier ($x = 0$) and strongly attenuated in distant regions. An increase of the permeability enhances the exchange between two subintervals and thus reduces the transverse magnetization peak around the barrier. At very high permeability ($\kappa = 10^{-3} \text{ m/s}$), the barrier has almost no influence onto diffusion, and the transverse magnetization is fully attenuated in this region. The strongest variation in the height of the transverse magnetization peak occurs when the permeability changes in the range between 10^{-5} m/s and 10^{-4} m/s , which is significant for biological tissues. In other words, the application of high gradients may allow for a more accurate permeability estimation.

3.4. PGSE signal: from Gaussian to stretched-exponential behavior

The transverse magnetization $M_t(x|g)$ which is not accessible at the experimental spatial resolution, was presented only for

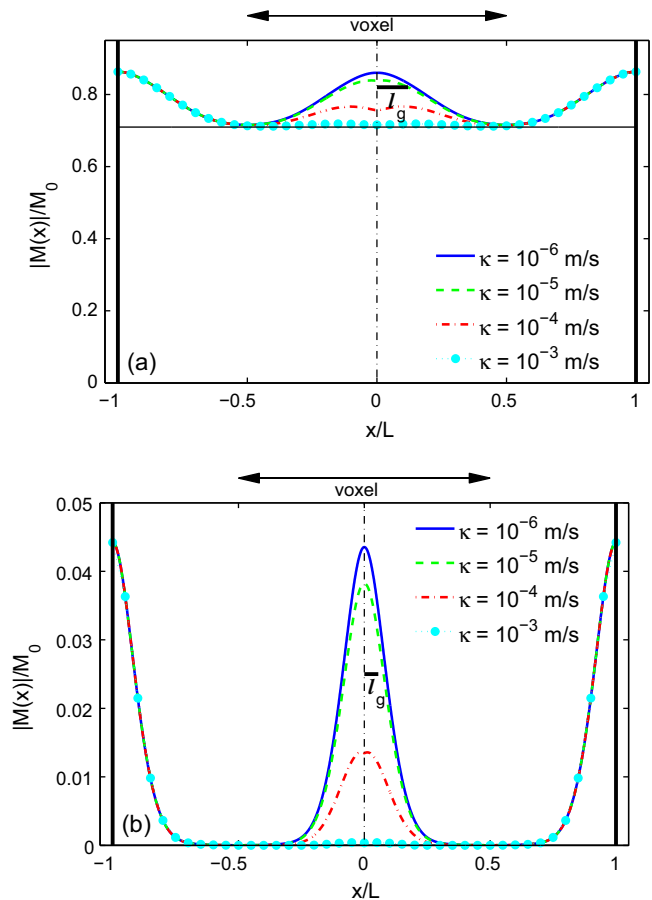


Fig. 4. The absolute value of the normalized transverse magnetization $M_{2\Delta}(x|g)/M_0$ at the echo time 2Δ for an interval $[-L, L]$ with two reflecting endpoints (thick vertical lines) and one semi-permeable barrier at the center (dash-dotted vertical line). The parameters are: $D = 2.3 \cdot 10^{-9} \text{ m}^2/\text{s}$, $\Delta = \delta = 50 \text{ ms}$, $L = 100 \mu\text{m}$, and $g = 5 \text{ mT/m}$ (a) and $g = 50 \text{ mT/m}$ (b). The initial transverse magnetization is uniformly distributed. Horizontal solid line shows the normalized transverse magnetization (i.e., the signal) for unrestricted diffusion ($\kappa = \infty$) which is not visible on (b). Thick bar indicates the gradient length l_g .

illustrative purposes. In turn, one can access the macroscopic PGSE signal $S(g)$ (i.e., the integral of the transverse magnetization $M_t(x|g)$) as a function of the gradient g , as shown by symbols in Fig. 5. At small g , $\ln S(g)$ exhibits the characteristic quadratic dependence on g . For comparison, dotted line presents the PGSE signal (21) for unrestricted diffusion (corresponding to infinite permeability).

The underlying Gaussian phase approximation breaks at g around 15 mT/m (Fig. 5a) and 200 mT/m (Fig. 5b). At higher gradients, the localization regime is established, with the non-Gaussian behavior $\ln S(g) \propto g^{2/3}$, according to Eq. (19). This behavior was derived by Stoller et al. for impermeable barriers ($\kappa = 0$) [54], and then extended to semi-permeable barriers in Section 2. Remarkably, the explicit asymptotic relation (19) accurately reproduces the PGSE signal for moderate permeabilities that makes the present study relevant not only for theoretical understanding of dMRI at high gradients but also for approximation and interpretation of PGSE signals.

For the highest permeability $\kappa = 10^{-3} \text{ m/s}$, the non-Gaussian behavior is established for gradients larger than 30 mT/m at which the signal attenuation is too strong ($S < 0.001$) that makes its experimental detection too challenging. For this reason, we ignored this situation (note also that so large permeability is not biologically relevant).

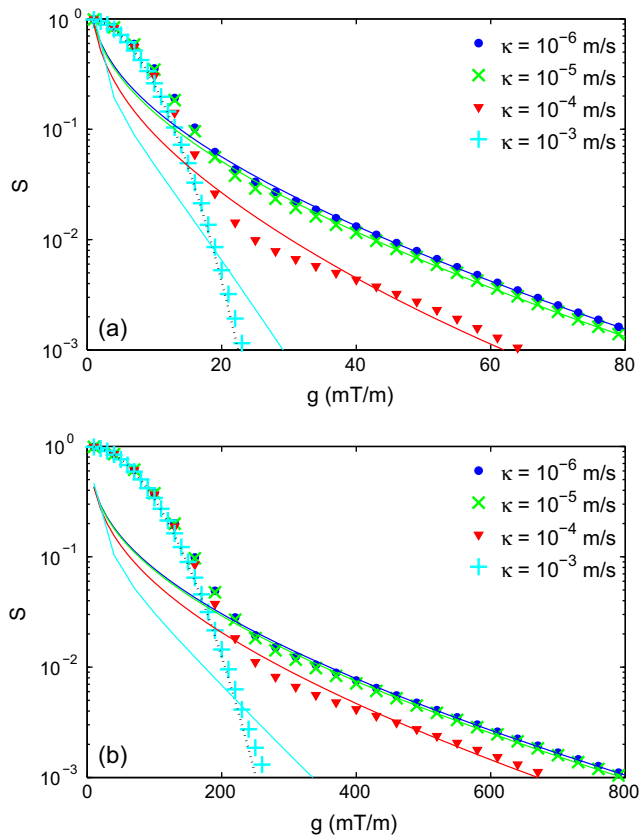


Fig. 5. PGSE signal as a function of the gradient g for an interval $[-L, L]$ with two reflecting endpoints and one semi-permeable barrier at the center. The parameters are: $D = 2.3 \cdot 10^{-9} \text{ m}^2/\text{s}$, $L = 100 \text{ }\mu\text{m}$, four values of κ : 10^{-6} m/s (circles), 10^{-5} m/s (crosses), 10^{-4} m/s (triangles), and 10^{-3} m/s (pluses), with $\Delta = \delta = 50 \text{ ms}$ (a) and $\Delta = \delta = 10 \text{ ms}$ (b). Solid lines indicate the long-time asymptotic behavior in Eq. (19). The initial transverse magnetization is uniformly distributed over the interval $[-L, L]$, while the signal is computed over the subinterval $[-R, R]$, with $R = 50 \text{ }\mu\text{m}$. Black dotted line shows the PGSE signal (21) for unrestricted diffusion ($\kappa = \infty$).

3.5. Higher sensitivity to permeability at high gradients

One can see in Fig. 5 that the asymptotic curves for different κ exhibit a similar dependence on g , being “shifted” along the vertical axis. The sensitivity of the PGSE signal to the permeability can be employed to estimate this quantity. In order to quantify this “shift”, we normalize the signal $S(g)$ for a given permeability κ by the signal $S_{\kappa=0}(g)$ with zero permeability. The ratio $S(g)/S_{\kappa=0}(g)$ as a function of the permeability κ is plotted in Fig. 6 for different gradient intensities. One can see that signals at higher gradients, at which the Gaussian phase approximation fails, are more sensitive to variations of κ . The strongest variation of the ratio occurs in the range of permeabilities between 10^{-5} m/s and 10^{-4} m/s . As we discussed above, the parameter h from Eq. (10) remains small for biologically relevant permeabilities so that the small- h asymptotics (16) yields in the long-time limit:

$$S(g) \simeq \frac{\zeta \rho_0}{(\gamma g/D)^{1/3}} \times \exp\left(-|a'_1|D^{1/3}(\gamma g)^{2/3}\delta - \kappa \frac{\sqrt{3}(\gamma g)^{1/3}}{|a'_1|D^{1/3}}\delta\right), \quad (22)$$

where $|a'_1| \approx 1.0188$. The “shift” in the signal can be mainly attributed to the second term containing κ , although the prefactor ζ also exhibits weak variations with κ (see Fig. 2). The approximate relation (22) is applicable at high gradients (when the localization regime holds) and moderate permeabilities (for which $h \ll 1$). Solid black line in Fig. 6 shows the approximate ratio

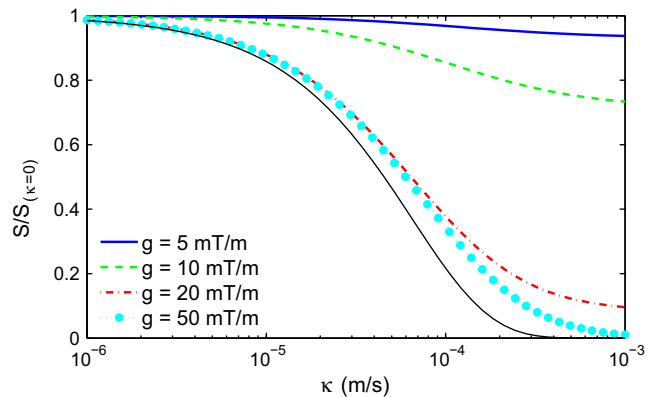


Fig. 6. Normalized PGSE signal $S(g)/S_{\kappa=0}(g)$ as a function of the permeability κ , for an interval $[-L, L]$ with two reflecting endpoints and one semi-permeable barrier at the center. The parameters are: $D = 2.3 \cdot 10^{-9} \text{ m}^2/\text{s}$, $\Delta = \delta = 50 \text{ ms}$, $L = 100 \text{ }\mu\text{m}$. The initial transverse magnetization is uniformly distributed over the interval $[-L, L]$, while the signal is computed over the subinterval $[-R, R]$, with $R = 50 \text{ }\mu\text{m}$. Signals at higher gradients are more sensitive to variations of κ . The normalization factor $S_{\kappa=0}(g)$ takes the values: 0.7632 ($g = 5 \text{ mT/m}$), 0.3561 ($g = 10 \text{ mT/m}$), 0.0549 ($g = 20 \text{ mT/m}$), and 0.0075 ($g = 50 \text{ mT/m}$). Solid black line indicates the ratio $S(g)/S_{\kappa=0}(g)$ from the approximate relation (22) for $g = 50 \text{ mT/m}$.

$S(g)/S_{\kappa=0}(g) \simeq \exp\left(-\kappa \frac{\sqrt{3}(\gamma g)^{1/3}}{|a'_1|D^{1/3}}\delta\right)$ for $g = 50 \text{ mT/m}$. One can see that this approximation is accurate at low permeabilities, while deviations emerge at high permeabilities at which h is not small (e.g., $h = 2.42$ at $\kappa = 10^{-3} \text{ m/s}$).

From theoretical point of view, the normalization by $S_{\kappa=0}(g)$ was performed to remove the prefactor and the leading term in the exponential function, and to highlight the stronger sensitivity of the PGSE signal to permeability as higher gradients. On experimental side, similar idea can potentially be realized in biological tissues by measuring two PGSE signals, before and after the action of aquaporin blockers that inhibit aquaporin water channels and thus significantly reduce the water permeability of cellular membranes [72–76].

3.6. Danger of phenomenological models

In medical applications, the PGSE signal is presented as a function of the b -value in order to stress the linear dependence of $\ln S$ at small gradients and possible deviations from linearity at larger gradients. Fig. 7 reproduces the PGSE signals from Fig. 5 for two permeabilities: $\kappa = 10^{-6} \text{ m/s}$ and $\kappa = 10^{-4} \text{ m/s}$. As expected from our analysis above, a linear slope of $\ln S$ at small b -values (Gaussian phase approximation) gradually changes to the $b^{1/3}$ behavior at high b -values (localization regime). Deviations from a linear slope have been reported in many experiments on dMRI of brain (see review [6] and references therein). The kurtosis and bi-exponential models are the most usual models for interpreting such experiments.

The kurtosis model relies on the perturbative expansion of the signal and includes the second-order term in b : $S_k = \exp(-bD_a + b^2(D_a)^2K_a/6)$, where D_a and K_a are apparent diffusion coefficient and apparent diffusion kurtosis [43]. Although the inclusion of the next-order (b^2) term allows one to account for weak deviations from the linear slope, the applicability range of this formula is obviously limited due to unphysical growth at large b . Higher-order moments can further be included but such models are impractical due to fitting problems. Moreover, the finite convergence radius of the cumulant expansion sets a fundamental limitation on the range of its applicability [41,49].

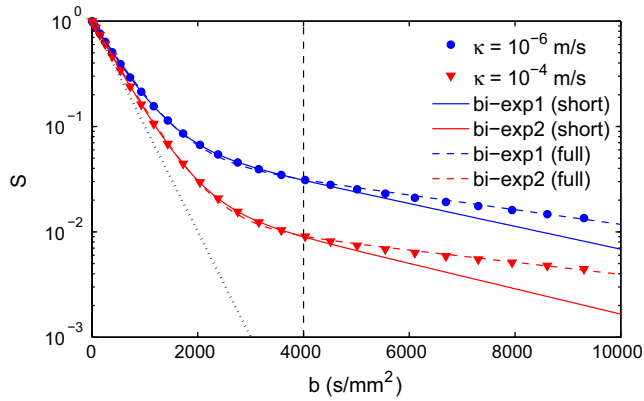


Fig. 7. Two PGSE signals S from Fig. 5a as a function of $b = \gamma^2 g^2 \delta^2 (\Delta - \delta/3)$ for two permeabilities, $\kappa = 10^{-6}$ m/s (circles) and $\kappa = 10^{-4}$ m/s (triangles), with $D = 2.3 \cdot 10^{-9}$ m²/s and $\Delta = \delta = 50$ ms. Dotted line indicates the signal for unrestricted diffusion. Two solid lines show, for each signal, its bi-exponential fit (23), obtained by a least squares method over b -values between 0 and 4000 s/mm² (see Table 1 for parameters). The bi-exponential function provides an excellent fit over its typical validity range (delimited by vertical dashed line) while strong deviations emerge at larger b -values. For comparison, two dashed lines show the bi-exponential fit of each signal obtained by a least squares method over the whole range of b -values, from 0 to 10,000 s/mm² (see Table 1). Once again, the bi-exponential fit is perfect for the whole range of b -values, although the parameters are different.

The bi-exponential model relies on the idea of two co-existing pools of water molecules exhibiting Gaussian diffusion with slow and fast diffusion coefficients D_{slow} and D_{fast} :

$$S_b = \alpha e^{-bD_{\text{fast}}} + (1 - \alpha)e^{-bD_{\text{slow}}}, \quad (23)$$

where α is the relative volume fraction of the fast pool. For typical range of applicability (between 0 and 4000 s/mm²), these two models often provide similarly good fits to experimental signals.

However, we emphasize that a good fit does not necessarily justify the applicability of the model and the consistence of the underlying interpretation [35,49]. We illustrate this point in Fig. 7, where two PGSE signals exhibiting transition to the localization regime, are fitted to a bi-exponential model on the range of b -values between 0 and 4000 s/mm². On this range, the bi-exponential model provides an excellent fit, though there is no microscopic justification for slow and fast diffusion pools. On the other hand, strong deviations from the bi-exponential model appear for larger b -values. In order to further highlight the ability of a bi-exponential fit to reproduce dMRI signals, we also fit the same signals over the whole range of b -values, from 0 to 10,000 s/mm² (dashed lines in Fig. 7). Once again, the bi-exponential fit is perfect over this extended range while the fit parameters are different (see Table 1). This example illustrates the danger of using phenomenological models without microscopic justifications.

It is tempting to interpret the transition to the localization regime as a possible explanation of experimentally observed deviations from the classical Gaussian behavior at high gradients (or b -values). However, this potential interpretation needs further

Table 1
Parameters of bi-exponential fits from Fig. 7 for $\kappa_1 = 10^{-6}$ m/s and $\kappa_2 = 10^{-4}$ m/s. Here “short” and “full” refer to two ranges of b -values used for fitting: 0–4000 s/mm² (“short”) and 0–10,000 s/mm² (“full”).

	Fit name	α	D_{fast} (ms/ μm^2)	D_{slow} (ms/ μm^2)
κ_1	bi-exp1 (short)	0.92	1.96	0.25
	bi-exp1 (full)	0.94	1.84	0.16
κ_2	bi-exp2 (short)	0.97	2.07	0.28
	bi-exp2 (full)	0.985	1.98	0.13

analysis to be justified and remains speculative at the present stage because of highly complicated microstructure of biological tissues. The relevance of the localization regime for lung dMRI has already been discussed [77].

3.7. Multiple semi-permeable barriers

The case of a single semi-permeable barrier is an idealized scheme for a better understanding of the mechanisms of signal formation at high gradients by analytical tools. In practice, a macroscopic voxel contains multiple microscopic barriers. The very rapid decay of the transverse magnetization far from the barrier allows one to consider many barriers independently if the inter-barrier distance ℓ_b is much larger than the gradient length ℓ_g . When the distance between adjacent barriers is not large, the transverse magnetizations near each barrier interfere and form a non-additive contribution to the signal. Here we illustrate this effect by considering two semi-permeable barriers of the same permeability κ , separated by distance ℓ_b . Although the transverse magnetization and the PGSE signal can be deduced from the propagator for which an exact solution is constructed in SM [60], we used the matrix formalism for multilayered structures [35]. Another illustration with 4 semi-permeable barriers is reported in SM [60].

Fig. 8 shows the absolute value of the transverse magnetization $M_{2\Delta}(x|g)$ at the echo time 2Δ , normalized by the initial magnetization M_0 . The parameters are $D = 2.3 \cdot 10^{-9}$ m²/s, $\Delta = \delta = 50$ ms. For two gradients $g = 5$ mT/m and $g = 50$ mT/m, the gradient length $\ell_g = (\gamma g/D)^{-1/3}$ is equal to 12.0 μm and 5.6 μm , respectively, while the diffusion length $\sqrt{2D\Delta}$ is 15 μm .

In Fig. 8a and c, the inter-barrier distance $\ell_b = 50$ μm is large as compared to the diffusion length $\sqrt{2D\Delta}$ so that water molecules rarely cross both barriers. As a consequence, two barriers affect the transverse magnetization almost independently, and one retrieves the patterns from Fig. 4 for a single barrier.

The situation changes when the inter-barrier distance ℓ_b is small (or comparable) to the diffusion length $\sqrt{2D\Delta}$. Even if the gradient length ℓ_g is small enough, rapid diffusion between two barriers reduces or fully destroys the localization effect. Fig. 8b and d illustrates this situation for $\ell_b = 10$ μm , for which the transverse magnetization is essentially flat even at high gradient $g = 50$ mT/m. At small permeability $\kappa = 10^{-6}$ m/s, the interior domain (between two barriers) does not almost exchange with the exterior space. Due to rapid diffusive equilibration inside the interior domain, the non-Gaussian localization regime is replaced by Gaussian motional narrowing regime [78,79]. For an isolated interval of length ℓ_b , the PGSE signal reads [78]

$$S_{\text{mn}}(g) \simeq \exp\left(-\frac{\gamma^2 g^2 \ell_b^4 (2\delta)}{120D}\right), \quad (24)$$

when the diffusion length is much larger than ℓ_b (see [3] for details). In particular, the transverse magnetization becomes $M_{2\Delta}(x|g) \approx M_0 S_{\text{mn}}(g)$, as illustrated in Fig. 8b and d by horizontal dashed line. Note that Eq. (24) can be deduced from the exact solution for two impermeable barriers in the limit of small g (see SM [60]). At higher permeabilities, faster diffusive exchange with the exterior space violates Eq. (24), and the level of nearly flat transverse magnetization is gradually reduced.

Since the PGSE signal is obtained by integrating the transverse magnetization over the voxel, contributions from different subdomains are superimposed. The relative contributions from short and long intervals can be comparable because higher amplitude of the transverse magnetization for short intervals is integrated over shorter domains. As a consequence, the dependence of the PGSE signal on the gradient can be rather complicated, being a superposition of Gaussian contributions from short intervals and

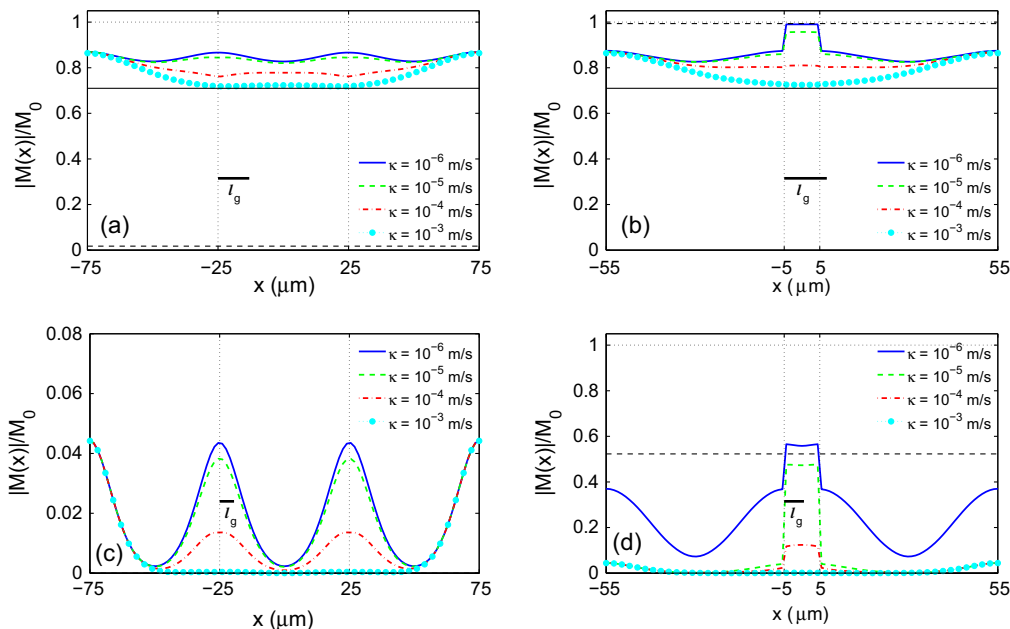


Fig. 8. The absolute value of the transverse magnetization $M_{2,\Delta}(x|g)$ at the echo time 2Δ , normalized by the initial magnetization M_0 , for two semi-permeable barriers indicated by vertical dotted lines. The parameters are: $D = 2.3 \cdot 10^{-9} \text{ m}^2/\text{s}$, $\Delta = \delta = 50 \text{ ms}$, $g = 5 \text{ mT/m}$ (a, b) and $g = 50 \text{ mT/m}$ (c, d), and the inter-barrier distance is $\ell_b = 50 \mu\text{m}$ (a, c) and $\ell_b = 10 \mu\text{m}$ (b, d). The thick bar shows the gradient length $\ell_g = (\gamma g/D)^{-1/3}$ which is equal to $12.0 \mu\text{m}$ (a, b) and $5.6 \mu\text{m}$ (c, d). The initial transverse magnetization is uniformly distributed over the interval $[-L - \ell_b/2, L + \ell_b/2]$ with reflecting endpoints so that $M_0 = 1/(2L + \ell_b)$, where $L = 50 \mu\text{m}$. Horizontal black line indicates the normalized magnetization $S_0(g)$ for unrestricted diffusion ($\kappa = \infty$), not visible on (c, d). Horizontal dashed line shows the normalized magnetization $S_{mn}(g)$ for motional narrowing regime from Eq. (24).

non-Gaussian contributions from long intervals. The general analytical formulas derived in SM [60] and the numerical matrix formalism allow one to investigate this behavior for any given configuration of multiple semi-permeable barriers. Note that the effect of spatial arrangement of semi-permeable barriers onto time-dependent diffusion coefficient was investigated by Novikov and co-workers [39]. Their analysis relied on a purely diffusive problem and is therefore relevant in the limit of small gradients. In contrast, our study focuses not only on the diffusive dynamics of the nuclei but essentially on the PGSE signal as an NMR tool for probing this dynamics. In this light, the influence of spatial disorder of barriers onto the PGSE signal remains almost unknown and presents a promising perspective for future research.

3.8. Three-dimensional domains

In this paper, we have employed analytical tools to investigate the emergence of stretched-exponential signal attenuation due to restricted motion of the nuclei near a single semi-permeable barrier at high gradients. The analysis essentially relied on the one-dimensional character of the problem for which an appropriate rescaling reduced the (Laplace-transformed) Bloch–Torrey equation to the Airy equation (see SM [60]). In higher dimensions, an applied gradient pins one direction that prevents a reduction to standard special functions even for such simple domains as disk or sphere. In other words, an exact analytical solution of the Bloch–Torrey equation is unavailable for nontrivial two- and three-dimensional domains. Numerical schemes such as finite-element or finite-difference methods, Monte Carlo simulations, and matrix formalisms remain the principal investigation tools [35,65–70,80–84] (see also review [3] and references therein). To our knowledge, the only exception is the work by de Swiet and Sen who performed an asymptotic analysis to demonstrate that the stretched-exponential behavior of the PGSE signal from the one-dimensional case remains valid for an isolated sphere in three dimensions [57]. Although similar analysis could be performed for a sphere with a semi-permeable surface, we merely focus on

illustrating the validity of the localization regime for three-dimensional domains.

First, we consider a three-dimensional semi-permeable plane which forms an angle θ with the applied gradient. Since the displacements of the nuclei in parallel and perpendicular directions to the plane are independent, the signal is the product between the classical attenuation factor $\exp(-D\gamma^2(g \sin \theta)^2 t^3/12)$ due to unrestricted lateral motion along the plane, and the signal S from Eqs. (18) or (19) due to restricted one-dimensional motion in the gradient $g \cos \theta$. Fig. 9 shows the dependence of the whole signal on the angle θ at small gradient $g = 5 \text{ mT/m}$ and high gradient $g = 30 \text{ mT/m}$ (with $\delta = \Delta = 50 \text{ ms}$). When the gradient is parallel to the plane ($\theta = 90^\circ$), one retrieves the Gaussian signal due to unrestricted diffusion which is negligible at $g = 30 \text{ mT/m}$. In turn, when the gradient is perpendicular to the plane ($\theta = 0$), one deals with the one-dimensional problem studied above, with either Gaussian behavior at small gradients (Fig. 9a), or stretched-exponential signal attenuation at high gradients (Fig. 9b). In other words, one can explore the transition between these two regimes by varying the angle θ . Although the signal is much more attenuated at high gradients, the effect of permeability is more pronounced in this situation. Note that similar anisotropic effects are broadly used for fiber tracking at small gradients when the Gaussian phase approximation holds. The present results indicate that larger gradients may be beneficial for revealing microscopic tissue anisotropy.

In general, a smooth curved membrane can be locally approximated by a flat plane if the radius of curvature is much larger than the diffusion length. In this way, the signal attenuation can be locally decomposed into restricted and unrestricted (Gaussian) factors as discussed above. The integral of these local contributions over surface points provides a first approximation to the overall signal. However, the dependence of the signal from one-dimensional restricted motion on the gradient is rather complicated, especially for semi-permeable barriers, that would make such an approximation impractical. At the same time, one can deduce an important qualitative conclusion: the signal is expected to be more

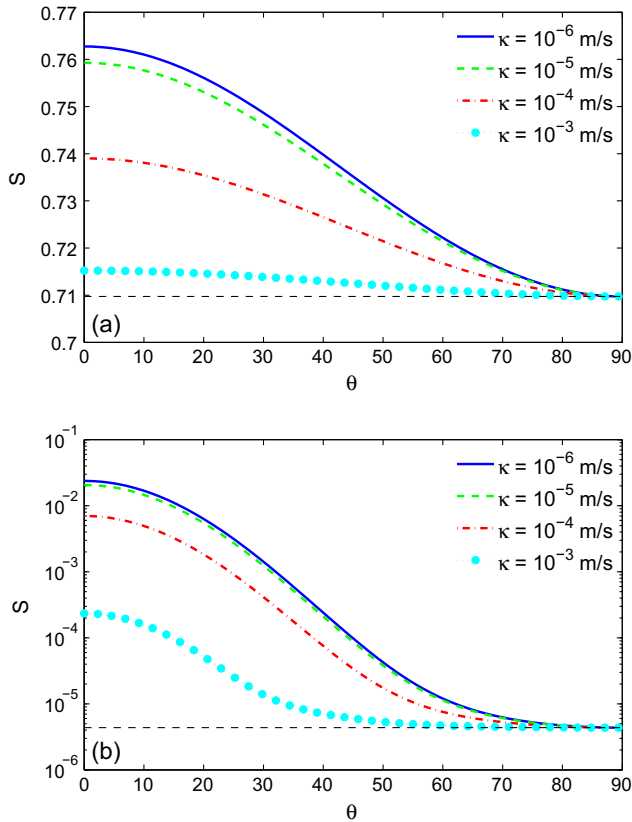


Fig. 9. PGSE signal as a function of the angle θ between the gradient and the normal vector to the plane, for $g = 5$ mT/m (a) and $g = 30$ mT/m (b). The parameters are: $D = 2.3 \cdot 10^{-9}$ m²/s and $\Delta = \delta = 50$ ms. Horizontal dashed line represents the PGSE signal for unrestricted diffusion (that corresponds to $\theta = 90^\circ$).

attenuated for nonflat membranes than for flat ones. In fact, when the membrane is not flat, the gradient cannot be chosen perpendicular to the barrier in all points so that lateral (Gaussian) attenuation factors in the signal are inevitable.

We illustrate this effect by considering a sphere with semi-permeable surface that allows for water exchange between the interior compartment and the exterior space. Fig. 10 shows the PGSE signal as a function of $(bD)^{1/3}$, for $D = 2.3 \cdot 10^{-9}$ m²/s, $\Delta = \delta = 50$ ms, g varying from 0 to 50 mT/m, $R = 50$ μ m (radius of sphere), and several permeabilities κ . The signal was computed numerically by a matrix formalism for multilayered structures [35]. For this purpose, we considered a sphere of radius R surrounded by a spherical shell with reflecting outer surface of radius $3R$. In order to exclude the effect of this artificial outer surface, the signal was computed by integrating the transverse magnetization over the spherical domain of radius $2R$. Since the diffusion length $\sqrt{2D\Delta} \approx 15$ μ m is much smaller than R , the contribution from the nuclei that hit the outer surface is negligible. For comparison, we also plot the PGSE signal for an isolated sphere of the same radius R , for which the exterior space is ignored (the signal is formed only by the nuclei inside the sphere).

For an isolated sphere (shown by pluses), one retrieves the localization regime at large gradients, as predicted by de Swiet and Sen [57]. The same trends are seen for a sphere with the exterior space, for both impermeable and semi-permeable barriers. Similarly to our observations for the one-dimensional case, there is a transition from the localization regime to Gaussian regime as the permeability increases. However, the localization regime is established when the signal is already strongly attenuated. As discussed above, the stronger attenuation results from less

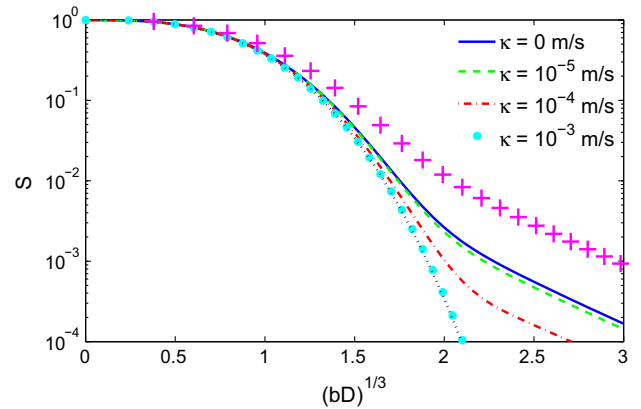


Fig. 10. PGSE signal as a function of $(bD)^{1/3}$ for a spherical barrier of radius $R = 50$ μ m and several permeabilities κ , with $b = \gamma^2 g^2 \delta^2 (\Delta - \delta/3)$. The parameters are: $D = 2.3 \cdot 10^{-9}$ m²/s, $\Delta = \delta = 50$ ms, and g varies from 0 to 50 mT/m. The initial transverse magnetization is uniformly distributed over the larger sphere of radius $3R$ with artificially introduced reflecting surface, while the signal is acquired over the smaller sphere of radius $2R$ to exclude the effect of this outer surface. For comparison, pluses show the PGSE signal for an isolated sphere of the same radius R .

restricted lateral motion for which the dephasing of nuclei is much stronger than that for more restricted perpendicular motion.

3.9. When does the localization regime emerge?

We summarize the conditions under which the leading terms with the smallest decay rate $|\text{Re}\{s_1\}|$ dominate over all other terms in the spectral decomposition (18), resulting in the localization regime and the non-Gaussian stretched-exponential decay (19) of the PGSE signal.

For a single impermeable barrier, the only condition is $\delta \gg \tau_g$ or, equivalently, $\ell_g \ll \sqrt{2D\delta}$, where ℓ_g and τ_g are defined by Eqs. (8) and (14). As $g \rightarrow 0$, the gradient length diverges, and the Gaussian behavior is necessarily recovered.

For a single semi-permeable barrier, the diffusive exchange should not be too strong that implies the second condition: $\ell_g \ll D/\kappa$ or, equivalently, $h \ll 1$, where h is defined in Eq. (10). In fact, for large h , the gap between the smallest $|\text{Re}\{s_1\}|$ and other $|\text{Re}\{s_n\}|$ becomes small [see Fig. 1 and the asymptotic relation (17)] so that many terms in Eq. (18) provide comparable contributions, “blurring” the stretched-exponential decay. In addition, the signal is much more attenuated as all $|\text{Re}\{s_n\}|$ are increased. This is the mathematical mechanism of the transition from the localization to Gaussian regime as h grows (either due to increasing κ or decreasing g).

Finally, when there are many barriers, the inter-barrier distance ℓ_b should be large compared to the diffusion length $\sqrt{2D\Delta}$ in order to maintain the localization mechanism and to get independent contributions from multiple barriers, as discussed in Section 3.7. In the opposite limit $\ell_b \ll \sqrt{2D\Delta}$, the Gaussian form (24) is recovered in the motional narrowing regime. Hürliemann et al. plotted a diagram of three regimes (almost free diffusion, motional narrowing regime, and localization regime), in terms of two ratios of the characteristic lengths: ℓ_g/ℓ_b and $\sqrt{2D\Delta}/\ell_b$ [58]. The present study extends this diagram into the third dimension by accounting for the diffusive exchange across barriers.

3.10. Does the localization regime matter?

Almost sixty years have passed since the formulation of the Bloch–Torrey equation [61]. During this period, diffusion MRI has become a routine experimental tool in medicine and material sciences [1–6], while numerous theoretical and numerical studies

have reinforced our understanding and interpretation of the acquired signals [3]. Theoretical research mainly relied either on the narrow pulse approximation (short gradient pulses), or on the Gaussian phase approximation (weak gradient amplitudes), while most practical attempts to correct for experimentally observed deviations from the familiar Gaussian behavior remained phenomenological. Amazingly, only few works dealt with high and long gradient pulses for which the localization regime was theoretically predicted and experimentally confirmed [54,57,58]. Why has this non-Gaussian behavior been ignored so far? Apart from rather involved mathematics and unconventional features of the localization regime, we discuss two reasons that might have hindered a better understanding of the localization regime and further developments of diffusion MRI at high gradients.

The mathematical reason originates from the spectral theory. It is well known that the Laplace operator governing pure diffusion is self-adjoint (or Hermitian) while its spectrum is discrete for bounded domains and continuum for unbounded domains [85]. Since the governing operator of the one-dimensional Bloch–Torrey equation, $\mathcal{L}_g = D\partial_x^2 + i\gamma gx$ (also known as complex Airy operator) is not Hermitian, standard tools and usual statements about spectral properties are not applicable. In particular, the existence and completeness of an eigenbasis are not granted, eigenvalues are not necessarily real, while the spectrum (if exists) may exhibit peculiar features (e.g., infinitely many branch points [54]). Our analysis in SM [60] suggests that the operator \mathcal{L}_g has a discrete spectrum for any, even *unbounded*, one-dimensional domain (except the whole line).¹ Strikingly, the inclusion of any obstacle (a barrier) or any gradient drastically changes the spectral properties of the operator \mathcal{L}_g , from a continuum spectrum for $g = 0$ (no gradient, pure diffusion) or $\kappa = \infty$ (no obstacle, whole line), to a discrete spectrum for $g > 0$ and $\kappa < \infty$. This explains the difficulty in understanding and quantifying the transition from the localization to Gaussian regime when the gradient g vanishes or the permeability κ diverges. For instance, as $g \rightarrow 0$, the spectral properties of \mathcal{L}_g cannot continuously approach that of the Laplace operator \mathcal{L}_0 for unbounded domains. Ironically, the classical Gaussian form of the PGSE signal which has found innumerable experimental applications and validations in dMRI, is a “pathological” (singular) limit of the non-perturbed solution of the one-dimensional Bloch–Torrey equation from the spectral point of view. This remark does not obviously discredit the practical usefulness of Gaussian signals but highlights our still limited understanding of the signal formation at high gradients.

In sharp contrast to the one-dimensional case, the governing operator $\mathcal{L}_g = D\Delta + i\gamma gx$ for unbounded domains *in higher dimensions* is expected to have a continuum spectrum for any g . This is obvious for a flat barrier in two or three dimensions for which the motions of nuclei in parallel (unrestricted) and perpendicular (restricted) directions to the barrier are decoupled. In practice, the localization regime in three-dimensional domains can still be relevant though possibly coupled to the Gaussian-type attenuation in lateral directions, as discussed in Section 3.8. Further mathematical analysis of this problem in two and three dimensions is important.

The physical reason for ignorance to the localization regime might be related to the need for an experimental setup with relatively high signal-to-noise ratio for reliable acquisition and interpretation of PGSE signals which are attenuated by at least one order of magnitude (or stronger). However, since the first experimental observation of the localization regime by Hürlimann et al. in 1995 [58], MRI scanners have been significantly improved. Nowadays, the limiting factors for observing the localization

regime in biological tissues can be the short inter-barrier distances and the coupling of the localization and Gaussian attenuation mechanisms due to nonflat three-dimensional structures of cellular membranes. In other words, although modern experimental setups allow one to observe the localization regime, the characteristic stretched-exponential decay of the PGSE signal can be superimposed with Gaussian decay and thus remain unnoticed.

So, does the localization regime matter in dMRI? Even if the one-dimensional setting of multiple barriers for which we derived the explicit formulas may look idealized, the localization mechanism and the consequent failure of the Gaussian phase approximation remain generic. The localization regime can emerge at gradients as moderate as 15–20 mT/m and thus be relevant under routinely used experimental conditions. Moreover, the current trend in increasing b -values is pushing experiments beyond the validity of the Gaussian phase approximation, thus requiring adequate mathematical tools and better understanding of the mechanisms of signal formation at high gradients. The present study makes a step in this direction by revealing the role of the diffusive exchange across barriers in the localization regime.

4. Conclusion

We presented a non-perturbative analytical approach for solving the one-dimensional Bloch–Torrey equation for diffusion across semi-permeable barriers. At high gradients, the transverse magnetization is localized near the barrier and very strongly attenuated in distant regions. In this localization regime, the Gaussian phase approximation fails, and the PGSE signal exhibits a non-Gaussian stretched-exponential decay, as first predicted by Stoller, Harper, and Dyson for impermeable barriers. Accounting for the diffusive exchange across the barrier enlarges the set of characteristic length scales of the problem and opens a new dimension for understanding the mechanisms of signal formation. In fact, varying the permeability, one can control the diffusive exchange and investigate the transition from the non-Gaussian behavior for weakly permeable barriers (small κ) to Gaussian behavior for highly permeable barriers (large κ). The ratio between the permeation length D/κ and the gradient length $(\gamma g/D)^{-1/3}$ has been identified as the major parameter determining the spectral properties. Although water exchange across semi-permeable membranes plays an important role in most biological structures, earlier studies of its influence onto the PGSE signal mainly relied on either the Gaussian phase approximation, or the narrow pulse approximation. The present approach is the first rigorous (non-perturbative) analysis at high gradients.

The analytical approach has been extended to an arbitrary configuration of semi-permeable barriers. When the inter-barrier distance is (much) larger than the diffusion length, different barriers can be treated separately and provide independent contributions to the PGSE signal. For instance, the localization regime can be relevant for large regularly arranged plant cells [86]. The gradient pulse duration δ should be large enough ($\delta \gg \tau_g$) to ensure the localization regime, and small enough ($\delta \ll \ell_b^2/D$) to prevent diffusive mixing between adjacent barriers. In turn, when two barriers are close, their localization effects onto the transverse magnetization interfere, and the Gaussian form of the PGSE signal is recovered in the motional narrowing regime. When both short and long inter-barrier gaps are present, the PGSE signal is a weighted superposition of Gaussian and non-Gaussian contributions. We also discussed the emergence of the localization regime for three-dimensional domains and showed the role of coupling between perpendicular and lateral motions of nuclei and the underlying mechanisms of signal attenuation.

Although our analysis remains largely theoretical, it prepares a mathematical ground for exploring new modalities in diffusion

¹ This statement is rigorously proved in [85] for a semi-axis with Dirichlet boundary condition. Similar proofs are expected to be applicable to other boundary conditions considered in this paper.

MRI. On one hand, proper accounting for the localization phenomenon can improve the physical interpretation of experimental measurements. For instance, we showed that a bi-exponential function can accurately fit the transition from Gaussian to non-Gaussian localization regime that illustrates the danger of using phenomenological models which rely only on fit quality. The explicit asymptotic relation (19), which accurately reproduces the PGSE signal for physiologically relevant permeabilities, can be used instead to approximate and interpret dMRI data at high gradients, at least for a simple situation of parallel barriers. Note that “high gradients” needed to observe the localization regime can be as low as 15–20 mT/m (for water diffusion) and thus easily available in conventional MRI scanners. The related mechanism of signal formation (with non-Gaussian stretched-exponential dependence on b -value) may therefore be relevant for current dMRI experiments in medicine (e.g., for brain and lungs) and in material sciences (e.g., for sedimentary rocks and cements). Moreover, it is tempting to interpret the transition to the localization regime as a possible explanation of experimentally observed deviations from the classical Gaussian behavior at high gradients. However, further analysis in complicated domains modeling the microstructure of biological tissues is needed to justify such an interpretation.

On the other hand, one can design new acquisition protocols profiting from the transverse magnetization localization and non-Gaussian features of the PGSE signal to reduce the acquisition time. In particular, high gradients are suitable to spatially localize the contribution of the nuclei near the barrier and thus estimate the barrier permeability. In fact, we showed the higher sensitivity of the PGSE signal to the permeability at high gradients. In a future work, the effect of the diffusion time Δ and of other temporal profiles (e.g., CPMG sequence, oscillating gradients, rectangular gradients with different gradients strengths/orientations, etc.) onto the localization regime can be analyzed. Such a study may help to answer the practically important question what are the “best” PGSE sequences to estimate the permeability in biological tissues.

Acknowledgment

The author acknowledges partial support by the Grant ANR-13-JSV5-0006-01 of the French National Research Agency.

References

- [1] P.T. Callaghan, Principles of Nuclear Magnetic Resonance Microscopy, Clarendon Press, Oxford, 1991.
- [2] W.S. Price, NMR Studies of Translational Motion: Principles and Applications, Cambridge University Press, 2009.
- [3] D.S. Grebenkov, NMR survey of reflected Brownian motion, *Rev. Mod. Phys.* 79 (2007) 1077–1137.
- [4] D.S. Tuch, T.G. Reese, M.R. Wiegell, V.J. Wedeen, Diffusion MRI of complex neural architecture, *Neuron* 40 (2003) 885–895.
- [5] J. Frahm, P. Dechent, J. Baudewig, K.D. Merboldt, Advances in functional MRI of the human brain, *Prog. Nucl. Magn. Reson. Spectrosc.* 44 (2004) 1–32.
- [6] D. Le Bihan, H. Johansen-Berg, Diffusion MRI at 25: exploring brain tissue structure and function, *NeuroImage* 61 (2012) 324–341.
- [7] T. Conlon, R. Outhred, Water diffusion permeability of erythrocytes using an NMR technique, *Biochim. Biophys. Acta* 288 (1972) 354–361.
- [8] J. Andrasko, Water diffusion permeability of human erythrocytes studied by a pulsed gradient NMR technique, *Biochim. Biophys. Acta* 428 (1976) 304–311.
- [9] J.E. Tanner, Transient diffusion in a system partitioned by permeable barriers. Application to NMR measurements with a pulsed field gradient, *J. Chem. Phys.* 69 (1978) 1748–1754.
- [10] K.R. Brownstein, C.E. Tarr, Importance of classical diffusion in NMR studies of water in biological cells, *Phys. Rev. A* 19 (1979) 2446–2453.
- [11] J. Kärgler, H. Pfeifer, W. Heink, Principles and applications of self-diffusion measurements by nuclear magnetic resonance, in: J.S. Waugh (Ed.), *Advances in Magnetic Resonance*, vol. 12, Academic Press, San Diego, CA, 1988, pp. 1–89.
- [12] M.D. Herbst, J.H. Goldstein, A review of water diffusion measurement by NMR in human red blood cells, *Am. J. Physiol. Cell Physiol.* 256 (1989) C1097–C1104.
- [13] J.E.M. Snaar, H. Van As, Probing water compartments and membrane permeability in plant cells by ^1H NMR relaxation measurements, *Biophys. J.* 63 (1992) 1654–1658.
- [14] J.G. Powles, M.J.D. Mallett, G. Rickayzen, W.A.B. Evans, Exact analytic solutions for diffusion impeded by an infinite array of partially permeable barriers, *Proc. R. Soc. London, Ser. A* 436 (1992) 391–403.
- [15] A. Szafer, J. Zhong, J.C. Gore, Theoretical model for water diffusion in tissues, *Magn. Reson. Med.* 33 (1995) 697–712.
- [16] A.V. Barzykin, K. Hayamizu, W.S. Price, M. Tachiyu, Pulsed-field-gradient NMR of diffusive transport through a spherical interface into an external medium containing a relaxation agent, *J. Magn. Reson. A* 114 (1995) 39–46.
- [17] J.C. Ford, D.B. Hackney, Numerical model for calculation of apparent diffusion coefficients (ADC) in permeable cylinders: comparison with measured ADC in spinal cord white matter, *Magn. Reson. Med.* 37 (1997) 387–394.
- [18] A.R. Waldeck, P.W. Kuchel, A.J. Lennon, B.E. Chapman, NMR diffusion measurements to characterize membrane transport and solute binding, *Prog. Nucl. Mag. Res. Spectrosc.* 30 (1997) 39–68.
- [19] G.J. Stanisz, A. Szafer, G.A. Wright, R.M. Henkelman, An analytical model of restricted diffusion in bovine optic nerve, *Magn. Reson. Med.* 37 (1997) 103–111.
- [20] G.J. Stanisz, J.G. Li, G.A. Wright, R.M. Henkelman, Water dynamics in human blood via combined measurements of T2 relaxation and diffusion in the presence of gadolinium, *Magn. Reson. Med.* 39 (1998) 223–233.
- [21] E.G. Novikov, D. van Dusschoten, H. van As, Modeling of self-diffusion and relaxation time NMR in multi-compartment systems, *J. Magn. Reson.* 135 (1998) 522–528.
- [22] W.S. Price, A.V. Barzykin, K. Hayamizu, M. Tachiyu, A model for diffusive transport through a spherical interface probed by pulsed-field gradient NMR, *Biophys. J.* 74 (1998) 2259–2271.
- [23] J. Pfeuffer, W. Dreher, E. Sykova, D. Leibfritz, Water signal attenuation in diffusion-weighted H NMR experiments during cerebral ischemia: influence of intracellular restrictions, extracellular tortuosity, and exchange, *Magn. Reson. Imaging* 16 (1998) 1023–1032.
- [24] P.W. Kuchel, C.J. Durrant, Permeability coefficients from NMR q-space data: models with unevenly spaced semi-permeable parallel membranes, *J. Magn. Reson.* 139 (1999) 258–272.
- [25] C.S. Landis, X. Li, F.W. Telang, P.E. Molina, I. Palyka, G. Vetek, C.S. Springer, Equilibrium transcytolemmal water-exchange kinetics in skeletal muscle in vivo, *Magn. Reson. Med.* 42 (1999) 467–478.
- [26] C.-L. Chin, F.W. Wehrli, S.N. Hwang, M. Takahashi, D.B. Hackney, Biexponential diffusion attenuation in the rat spinal cord: computer simulations based on anatomic images of axonal architecture, *Magn. Reson. Med.* 47 (2002) 455–460.
- [27] J.D. Quirk, G.L. Bretthorst, T.Q. Duong, A.Z. Snyder, C.S. Springer, J.J.H. Ackerman, J.J. Neil, Equilibrium water exchange between the intra- and extracellular spaces of mammalian brain, *Magn. Reson. Med.* 50 (2003) 493–499.
- [28] C. Meier, W. Dreher, D. Leibfritz, Diffusion in compartmental systems. I. A comparison of an analytical model with simulations, *Magn. Reson. Med.* 50 (2003) 500–509.
- [29] G.J. Stanisz, Diffusion MR in biological systems: tissue compartments and exchange, *Isr. J. Chem.* 43 (2003) 33–44.
- [30] A.L. Sukstanskii, D.A. Yablonskiy, J.J.H. Ackerman, Effects of permeable boundaries on the diffusion-attenuated MR signal: insights from a one-dimensional model, *J. Magn. Reson.* 170 (2004) 56–66.
- [31] Y. Assaf, R.Z. Freidlin, G.K. Rohde, P.J. Basser, New modeling and experimental framework to characterize hindered and restricted water diffusion in brain white matter, *Magn. Reson. Med.* 52 (2004) 965–978.
- [32] P.N. Sen, P.J. Basser, Modeling diffusion in white matter in the brain: a composite porous medium, *Magn. Reson. Imaging* 23 (2005) 215–220.
- [33] M. Parisi, R.A. Dorr, M. Ozu, R. Toriano, From membrane pores to aquaporins: 50 years measuring water fluxes, *J. Biol. Phys.* 33 (2007) 331–343.
- [34] I. Åslund, A. Nowacka, M. Nilsson, D. Topgaard, Filter-exchange PGSE NMR determination of cell membrane permeability, *J. Magn. Reson.* 200 (2009) 291–295.
- [35] D.S. Grebenkov, Pulsed-gradient spin-echo monitoring of restricted diffusion in multilayered structures, *J. Magn. Reson.* 205 (2010) 181–195.
- [36] D.S. Grebenkov, Use, misuse and abuse of apparent diffusion coefficients, *Conc. Magn. Reson. A* 36 (2010) 24–35.
- [37] E. Fieremans, D.S. Novikov, J.H. Jensen, J.A. Helpert, Monte Carlo study of a two-compartment exchange model of diffusion, *NMR Biomed.* 23 (2010) 711–724.
- [38] D.A. Yablonskiy, A.L. Sukstanskii, Theoretical models of the diffusion weighted MR signal, *NMR Biomed.* 23 (2010) 661–681.
- [39] D.S. Novikov, E. Fieremans, J.H. Jensen, J.A. Helpert, Random walks with barriers, *Nat. Phys.* 7 (2011) 508–514.
- [40] D.S. Grebenkov, D.V. Nguyen, J.-R. Li, Exploring diffusion across permeable barriers at high gradients. I. Narrow pulse approximation, *J. Magn. Reson.* 248 (2014) 153–163.
- [41] A.F. Fröhlich, L. Østergaard, V.G. Kiselev, Effect of impermeable boundaries on diffusion-attenuated MR signal, *J. Magn. Reson.* 179 (2006) 223–233.
- [42] V.G. Kiselev, The cumulant expansion: an overarching mathematical framework for understanding diffusion NMR, in: D.K. Jones (Ed.), *Diffusion MRI: Theory, Methods and Applications*, Oxford University Press, Oxford, 2010 (Chapter 10).
- [43] J.H. Jensen, J.A. Helpert, A. Ramani, H. Lu, K. Kaczynski, Diffusional kurtosis imaging: the quantification of non-Gaussian water diffusion by means of magnetic resonance imaging, *Magn. Reson. Med.* 53 (2005) 1432–1440.
- [44] R. Trampel, J.H. Jensen, R.F. Lee, I. Kamenetskiy, G. McGuinness, G. Johnson, Diffusional Kurtosis imaging in the lung using hyperpolarized ^3He , *Magn. Reson. Med.* 56 (2006) 733–737.

- [45] T. Niendorf, R.M. Dijkhuizen, D.S. Norris, M. van Lookeren Campagne, K. Nicolay, Biexponential diffusion attenuation in various states of brain tissue: implications for diffusion-weighted imaging, *Magn. Reson. Med.* 36 (1996) 847–857.
- [46] R.V. Mulkern, H. Gudbjartsson, C.F. Westin, H.P. Zengingonul, W. Gartner, C.R. Guttmann, et al., Multicomponent apparent diffusion coefficients in human brain, *NMR Biomed.* 12 (1999) 51–62.
- [47] C.A. Clark, D. Le Bihan, Water diffusion compartmentation and anisotropy at high b values in the human brain, *Magn. Reson. Med.* 44 (2000) 852–859.
- [48] J.V. Sehy, J.J.H. Ackerman, J.J. Neil, Evidence that both fast and slow water ADC components arise from intracellular space, *Magn. Reson. Med.* 48 (2002) 765–770.
- [49] V.G. Kiselev, K.A. Il'yasov, Is the biexponential diffusion bilexponential?, *Magn. Reson. Med.* 57 (2007) 464–469.
- [50] M. Peyron, G.K. Pierens, A.J. Lucas, L.D. Hall, R.C. Stewart, The modified stretched-exponential model for characterization of NMR relaxation in porous media, *J. Magn. Reson. A* 118 (1996) 214–220.
- [51] K.M. Bennett, K.M. Schmainda, R. Bennett, D.B. Rowe, H. Lu, J.S. Hyde, Characterization of continuously distributed cortical water diffusion fates with a stretched-exponential model, *Magn. Reson. Med.* 50 (2003) 727–734.
- [52] D.A. Yablonskiy, A.L. Sukstanskii, J.C. Leawoods, D.S. Gierada, G.L. Bretthorst, S.S. Lefrak, J.D. Cooper, M.S. Conradi, Quantitative in vivo assessment of lung microstructure at the alveolar level with hyperpolarized He-3 diffusion MRI, *Proc. Natl. Acad. Sci. USA* 99 (2002) 3111–3116.
- [53] R.E. Jacob, G. Laicher, K.R. Minard, 3D MRI of non-Gaussian 3He gas diffusion in the rat lung, *J. Magn. Reson.* 188 (2007) 357–366.
- [54] S.D. Stoller, W. Happer, F.J. Dyson, Transverse spin relaxation in inhomogeneous magnetic fields, *Phys. Rev. A* 44 (1991) 7459–7477.
- [55] T.M. de Swiet, Diffusive edge enhancement in imaging, *J. Magn. Reson. B* 109 (1995) 12–18.
- [56] P.T. Callaghan, A. Coy, L.C. Forde, C.J. Rofe, Diffusive relaxation and edge enhancement in NMR microscopy, *J. Magn. Reson. A* 101 (1993) 347–350.
- [57] T.M. de Swiet, P.N. Sen, Decay of nuclear magnetization by bounded diffusion in a constant field gradient, *J. Chem. Phys.* 100 (1994) 5597–5604.
- [58] M.D. Hürlimann, K.G. Helmer, T.M. de Swiet, P.N. Sen, C.H. Sotak, Spin echoes in a constant gradient and in the presence of simple restriction, *J. Magn. Reson. A* 113 (1995) 260–264.
- [59] S. Axelrod, P.N. Sen, Nuclear magnetic resonance spin echoes for restricted diffusion in an inhomogeneous field: Methods and asymptotic regimes, *J. Chem. Phys.* 114 (2001) 6878–6895.
- [60] **Supplementary Materials.**
- [61] H.C. Torrey, Bloch equations with diffusion terms, *Phys. Rev.* 104 (1956) 563–565.
- [62] M. Abramowitz, I.A. Stegun, *Handbook of Mathematical Functions*, Dover Publisher, New York, 1965.
- [63] Y. Assaf, P.J. Basser, Composite hindered and restricted model of diffusion (CHARMED) MR imaging of the human brain, *NeuroImage* 27 (2005) 48–58.
- [64] E.O. Stejskal, J.E. Tanner, Spin diffusion measurements: spin echoes in the presence of a time-dependent field gradient, *J. Chem. Phys.* 42 (1965) 288–292.
- [65] A. Caprihan, L.Z. Wang, E. Fukushima, A multiple-narrow-pulse approximation for restricted diffusion in a time-varying field gradient, *J. Magn. Reson. A* 118 (1996) 94–102.
- [66] P.T. Callaghan, A simple matrix formalism for spin echo analysis of restricted diffusion under generalized gradient waveforms, *J. Magn. Reson.* 129 (1997) 74–84.
- [67] A.V. Barzykin, Exact solution of the Torrey–Bloch equation for a spin echo in restricted geometries, *Phys. Rev. B* 58 (1998) 14171–14174.
- [68] A.V. Barzykin, Theory of spin echo in restricted geometries under a step-wise gradient pulse sequence, *J. Magn. Reson.* 139 (1999) 342–353.
- [69] A.L. Sukstanskii, D.A. Yablonskiy, Effects of restricted diffusion on MR signal formation, *J. Magn. Reson.* 157 (2002) 92–105.
- [70] D.S. Grebenkov, Laplacian eigenfunctions in NMR I. A numerical tool, *Conc. Magn. Reson.* 32A (2008) 277–301.
- [71] D.S. Grebenkov, Laplacian eigenfunctions in NMR. II. Theoretical advances, *Conc. Magn. Reson.* 34A (2009) 264–296.
- [72] G.M. Preston, T.P. Carroll, W.B. Guggino, P. Agre, Appearance of water channels in Xenopus oocytes expressing red cell CHIP28 protein, *Science* 256 (1992) 385–387.
- [73] B.L. de Groot, H. Grubmüller, Water permeation across biological membranes: mechanism and dynamics of Aquaporin-1 and GlpF, *Science* 294 (2001) 2353–2357.
- [74] L.S. King, D. Kozono, P. Agre, From structure to disease: the evolving tale of aquaporin biology, *Nat. Rev. Mol. Cell Biol.* 5 (2004) 687–698.
- [75] A. Verkman, More than just water channels: unexpected cellular roles of aquaporins, *J. Cell Sci.* 118 (2005) 3225–3232.
- [76] D. Seeliger, C. Zapater, D. Krenc, R. Haddoub, S. Flitsch, E. Beitz, J. Cerda, B.L. de Groot, Discovery of novel human aquaporin-1 blockers, *ACS Chem. Biol.* 8 (2013) 249–256.
- [77] D.S. Grebenkov, G. Guillot, B. Sapoval, Restricted diffusion in a model acinar labyrinth by NMR. Theoretical and numerical results, *J. Magn. Reson.* 184 (2007) 143–156.
- [78] B. Robertson, Spin-echo decay of spins diffusion in a bounded region, *Phys. Rev.* 151 (1966) 273–277.
- [79] C.H. Neuman, Spin echo of spins diffusion in a bounded medium, *J. Chem. Phys.* 60 (1974) 4508–4511.
- [80] B. Balinov, B. Jönsson, P. Linse, O. Söderman, The NMR self-diffusion method applied to restricted diffusion. Simulation of echo attenuation from molecules in spheres and between planes, *J. Magn. Reson. A* 104 (1993) 17–25.
- [81] S.N. Hwang, C.L. Chin, F.W. Wehrli, D.B. Hackney, An image-based finite difference model for simulating restricted diffusion, *Magn. Reson. Med.* 50 (2003) 373–382.
- [82] J. Xu, M.D. Does, J.C. Gore, Numerical study of water diffusion in biological tissues using an improved finite difference method, *Phys. Med. Biol.* 52 (2007) N111–N126.
- [83] D.S. Grebenkov, A fast random walk algorithm for computing the pulsed-gradient spin-echo signal in multiscale porous media, *J. Magn. Reson.* 208 (2011) 243–255.
- [84] D.V. Nguyen, J.-R. Li, D.S. Grebenkov, D. Le Bihan, An efficient finite-elements code to simulate diffusion MRI signals in complex tissue geometries, *J. Comput. Phys.* 263 (2014) 283–302.
- [85] B. Helffer, *Spectral theory and its applications*, Cambridge Studies in Advanced Mathematics, vol. 139, Cambridge University Press, Cambridge, 2013.
- [86] H. Van As, Intact plant MRI for the study of cell water relations, membrane permeability, cell-to-cell and long-distance water transport, *J. Exp. Botany* 58 (2007) 743–756.